



HAL
open science

Simultaneous cathodoluminescence and electron microscopy cytometry of cellular vesicles labeled with fluorescent nanodiamonds

Sounderya Nagarajan, Catherine Pioche-Durieu, Luiz Tizei, Chia-Yi Fang, Jean-Rémi Bertrand, Eric Le Cam, Huan-Cheng Chang, François Treussart, Mathieu Kociak

► To cite this version:

Sounderya Nagarajan, Catherine Pioche-Durieu, Luiz Tizei, Chia-Yi Fang, Jean-Rémi Bertrand, et al.. Simultaneous cathodoluminescence and electron microscopy cytometry of cellular vesicles labeled with fluorescent nanodiamonds. *Nanoscale*, 2016, 8 (22), pp.11588-11594. 10.1039/c6nr01908k . hal-03065147

HAL Id: hal-03065147

<https://hal.science/hal-03065147>

Submitted on 22 Dec 2020

HAL is a multi-disciplinary open access archive for the deposit and dissemination of scientific research documents, whether they are published or not. The documents may come from teaching and research institutions in France or abroad, or from public or private research centers.

L'archive ouverte pluridisciplinaire **HAL**, est destinée au dépôt et à la diffusion de documents scientifiques de niveau recherche, publiés ou non, émanant des établissements d'enseignement et de recherche français ou étrangers, des laboratoires publics ou privés.

Simultaneous cathodoluminescence and electron microscopy cytometry of cellular vesicles labeled with fluorescent nanodiamonds

Sounderya Nagarajan,[†] Catherine Pioche-Durieu,[‡] Luiz H. G. Tizei,[†] Chia-Yi Fang,[§] Jean-Remi Bertrand,^{||} Eric Le Cam,[‡] Huan-Cheng Chang,[§] Francois Treussart,^{*,⊥} and Mathieu Kociak^{*,†}

[†] Laboratoire de Physique des Solides, CNRS, Univ. Paris-Sud, Université Paris-Saclay, 91405 Orsay, France

[‡] Signalisations, Noyaux et Innovations en Cancérologie, CNRS, Univ. Paris-Sud, Gustave Roussy, Université Paris-Saclay, 94805 Villejuif, France

[§] Institute of Atomic and Molecular Sciences, Academia Sinica, Taipei 106, Taiwan.

^{||} Laboratoire de Vectorologie et Thérapeutiques Anticancéreuses, UMR8203, CNRS, Univ. Paris-Sud, Gustave Roussy, Université Paris-Saclay, 94805 Villejuif, France

[⊥] Laboratoire Aimé Cotton, CNRS, Univ. Paris-Sud, ENS Cachan, Université Paris-Saclay, 91405 Orsay, France

AUTHOR INFORMATION

Corresponding Authors

*Email: mathieu.kociak@u-psud.fr and francois.treussart@ens-cachan.fr

Author Contributions

S.N., J.R.B., C.D., E.L.C., F.T., and M.K. conceived and designed the experiments; S.N., L.H.G.T., J.R.B., C.D., and M.K. performed the experiments; S.N., C.D., E.L.C., F.T. and M.K. analyzed the data; C.Y.F. and H.C.C. contributed materials/analysis tools; S.N., F.T. and M.K. co-wrote the paper.

Notes

The authors declare no competing financial interests.

Abstract

Light and Transmission Electron Microscopies (LM and TEM) hold potential in bioimaging owing to the advantages of fast imaging of multiple cells with LM and ultrastructure resolution offered by TEM. Integrated or Correlated LM and TEM are the current approaches to combine the advantages of both techniques. Here we propose an alternative in which the electron beam of a scanning TEM (STEM) is used to excite concomitantly the luminescence of nanoparticle labels (a process known as cathodoluminescence, CL), and image the cell ultrastructure. This CL-STEM imaging allows obtaining luminescence spectra and imaging ultrastructure simultaneously. We present a proof of principle experiment, showing the potential of this technique in image cytometry of cell vesicular components. To label the vesicles we used fluorescent diamond nanocrystals (nanodiamonds, NDs) of size ≈ 150 nm coated with different cationic polymers, known to trigger different internalization pathways. Each polymer was associated to a type of ND with different emission spectrum. With CL-STEM, for each individual vesicle, we were able to measure (i) their size with nanometric resolution, (ii) their content in different ND labels, and realize intracellular components cytometry. Contrary to the recently reported organelle flow cytometry technique that requires cell sonication, CL-STEM-based image cytometry preserves the cell integrity and provides a much higher resolution in size. Although this novel approach is still limited by a low throughput, the automatization of data acquisition and image analysis, combined with improved intracellular targeting, should facilitate applications in cell biology at the subcellular level.

Cell imaging techniques have been constantly evolving. Fluorescence microscopy is most widely used, owing to the possibility to label cell compartments with high specificity by immunofluorescence or by the expression of fluorescent proteins. In the last decades fluorescence-based super-resolution microscopies have opened new perspectives in structural imaging¹⁻³. This is particularly true in studying cellular dynamics and a striking example is the monitoring of endocytotic pits and actin filaments formation imaged at a resolution of 84 nm by structured illumination microscopy⁴. However, there still exist complexities in sample preparation, choice of fluorophores and difficulties in imaging the cellular morphology at sub-organelle resolution, despite these recent progresses.

On the contrary, electron microscopy (EM) easily reaches this spatial resolution when conducting structural investigations. Techniques where fluorescence and EM imaging can be correlated on the same sample, usually coined Correlative Light and Electron Microscopy (CLEM), have shown great success in recent years and are becoming standard⁵. Moreover, with the recent development of genetically encoded tags providing both EM and LM contrasts⁶ and complementing advantageously immunochemical nanogold labeling⁷, the gap between EM and LM is about to be bridged.

These methods utilizing both electron and light microscopies are implemented either independently or in correlative or integrated manners⁸. In conventional CLEM, samples are transferred between the light and the electron microscopes. This approach requires locating the same region of interest with fiducial markers⁹, which is not straightforward as there are non-linear distortions of the images due to various scanning systems. Integrated light and electron microscopy tries to get around these issues by using a fluorescence detection set up fitted on an electron microscope⁹, but it requires a light source aligned with the electron beam to excite the emitters.

An interesting alternative is to use electrons not only for structural imaging, but also to take advantage of the luminescence of some materials when they are probed with an accelerated electron beam, an effect known as cathodoluminescence (CL)¹⁰. This implies that the CL emission from the sample can be collected while it is imaged by an electron microscope without the need to move it from EM to LM setup. This approach has been used via the combination of CL and secondary electron scanning EM (SEM) for simultaneous luminescence and structural imaging of fluorescent rare-earth-doped yttrium or gadolinium oxide (Y_2O_3 or Gd_2O_3) particles after their uptake in cells^{11,12} and europium-zinc-codoped Y_2O_3 nanoparticles of size down to 30 nm¹³. Although SEM combined with CL (SEM-CL) provides a sub-cellular resolution¹¹, it is not sufficient for determining cell ultrastructure. On the other hand, Scanning Transmission Electron Microscopy (STEM) offers such an ultrastructural resolution, and it is thus appealing to extend SEM-CL to STEM-CL so as to get both ultrastructure and luminescence information in parallel. Indeed we demonstrated recently that STEM-CL is sensitive enough to address single nanoparticles, such as individual ≈ 20 nm sized core/shell quantum dots¹⁴ or ≈ 100 nm sized nanodiamonds (NDs) with embedded defect centers^{10,15}. In our CL-STEM configuration, the light collected is spectrally analyzed at each beam position, yielding one CL spectrum per pixel, and the matrix of CL spectrum is called a hyperspectral image.

NDs are actually remarkable STEM-CL labels owing to the large quantum yield and low electrobleaching of the embedded luminescent defects. Moreover, we have used cationic polymer-coated NDs to deliver gene to Ewing sarcoma cells in culture¹⁶ and have shown, in this context, that the internalization pathways and therefore the corresponding vesicular compartment labeled by the fluorescent ND (size ≈ 50 nm), depends on the cationic molecules used¹⁷: the Polyallylamine Hydrochloride (PAH) coating triggers clathrin-mediated endocytosis, whereas both clathrin-mediated endocytosis and macropinocytosis are involved in the case of Polyethylene Imine (PEI) coating, with a predominance for macropinocytosis. Such coated NDs are thus interesting labels of different internalization pathways.

In this Letter, we report a novel ultrastructural image cytometry method to investigate quantitatively the cellular uptake of nanoparticles. Our approach relies on the combination of STEM-CL imaging with fluorescent NDs having different spectral signatures for each type of cationic coating. We applied our method to some quantitative characterization of the compartments containing ND uptaken by human Ewing sarcoma cells A673 in culture. We studied single (ND-PEI or ND-PAH alone) and double labeling (both types of cationic ND put together) situations. Four hours after their cellular uptake, all NDs localized inside vesicles and were not found free in the cytoplasm. From ultrastructure images, we inferred the size of individual ND-containing vesicles, and used the ultrastructure-correlated CL emission to count the number of fluorescent NDs inside each vesicle. These counts are equivalent to luminescence intensities in conventional cytometry. For each vesicle we get a set of data made of its size, the number and the type (PEI, PAH or mixed PEI/PAH coating) of cationic NDs it contains. These data allowed us to build plots offering a synthetic view of all the information at the vesicle scale. Being based on ultrastructural imaging our novel cytometry is a method that could be further developed by extracting information, beyond the vesicle size.

Results and Discussion

We have used NDs with diameters ≈ 150 nm (see Supporting Information) containing nominally either Nitrogen Vacancy (NV) color centers (further referred as Type 1 NDs), having a red CL emission¹⁵ or Nitrogen Vacancy Nitrogen color centers (H3) with a green CL emission¹⁵ (further referred as Type 2 NDs). Type 1 NDs are made from synthetic precursors while the Type 2 NDs are made from natural diamond, which implies a better control of nitrogen impurity in Type 1 NDs than in Type 2 NDs. We observed that Type 1 NDs were pure red emitters while Type 2 ND sample was composed of a mixture of either green or red emitting NDs. We measured the content of pure green emitting NDs in Type 2 sample and found it to be 57 ± 2 % (Supporting Information Figure S1), with the rest (43%) being composed of NDs with a pure red emission. We also observed that ND in both samples had crystals that did not show any luminescence. We measured the fraction of fluorescent NDs to be 67 ± 5 % for Type 1 and 62 ± 3 % for Type 2.

Type 1 NDs were coated with PAH, (ND-PAH) and Type 2 NDs with PEI (ND-PEI). We incubated these cationic polymer-coated NDs with A673 cells, either separately or in conjunction (see Methods). The polymer coated NDs were spontaneously taken up by cells, and we then analyzed their intracellular distribution by STEM and CL-hyperspectral imaging. STEM enables imaging at the scale of a whole cell (Figure 1A) down to the ultrastructure (Figure 1B), in either a Bright Field (BF) mode with contrasts similar to that of conventional TEM, or High Angle Annular Dark Field (HAADF) with roughly speaking an inversed contrast. In both modes, subcellular compartments like mitochondria, lysosomes, endosomes and nuclear membranes, and at the same time NDs, are observed with a high contrast. NDs appear as black or white features in either BF or HAADF mode respectively. Figure 1C displays the detection system: the two images are obtained by scanning an electron beam (acceleration voltage ≈ 60 kV) onto the sample, and collecting the BF and the HAADF signal at each scan position. At the same time, a CL spectrum, showing clear NV or H3 signatures (Figure 1D) is collected at each scan position. The NV signature presents a well-known form, consisting in a Zero Phonon Line (ZPL) centered on 575 nm wavelength (corresponding to the neutral form¹⁸ NV⁰ followed by a convoluted series of peaks corresponding to phonon replica). Various analyses can be performed on this set of data (later called a spectrum image, Spim). The most straightforward method is to integrate the intensity in a given wavelength range (Figure 1D) for every pixel of the Spim and map this intensity to each point of the scan, producing colored images. This colored image can be related, pixel-by-pixel, to the morphological images (either BF or HAADF). As shown in Figure 1E, it is possible to correlate the emission properties of the fluorescent NDs and the samples ultrastructure (the vesicles) with nanometer resolution. However, while the green color unambiguously identifies a ND-PEI, a red emission might be attributed to a PAH or a PEI coated ND, due to non purity of Type 2 sample. Fortunately, the exact spectral shape can be used to disentangle both cases. Figure 2 shows that for known samples of ND-PEI and ND-PAH their CL spectra significantly differ in the ratio of ZPL to the phonon side band and in the phonon sideband shape too. These differences are visible only after PEI and PAH coating of the NDs and can be used for segregating red emitting NDs in ND-PAH and ND-PEI. To do so, we took advantage of the large redundancy of the data in spectral-imaging to analyze the data through multivariate analysis (see Supporting Information). We obtained 60% identification efficiency for ND-PAH and 100% for ND-PEI. The influence of the polycation coating on the CL spectra shape maybe related to band bending effect induced by electrophilic surface functionalization, as reported for hydrogenated diamond surface^{19,20}. Band bending results in a decrease of occupancy of NV in the vicinity of ND surface, depending on the electron affinity of the coating. Band bending effect on the phonon lines is however not documented in the literature and requires more detailed studies, out of scope of the present paper. From now on, we will thus only mention the type of coatings, as deduced from spectral analysis, without referring anymore to the type of embedded defect centers.

We then investigated the distribution of ND-PEI and ND-PAH inside the cells in different incubation conditions: when the cells are incubated (i) with ND-PAH alone, (ii) with ND-PEI alone at the same nominal concentration as ND-PAH, and (iii) when the cells are co-incubated with both ND-PAH and ND-PEI simultaneously, each of them at the same concentration as in (i) and (ii), so that in condition (iii) there is twice more NDs than in (i) and (ii). NDs were always found inside vesicular compartments and never free in the cytoplasm. From bright field and dark field images, we inferred the size of the vesicles, given as an equivalent diameter calculated as the geometric mean of the major and minor axis of its best approximant ellipse, and from the CL spectra we categorized the vesicle labeling depending on the type of coating of the NDs it contains. The number of NDs per vesicle varied between 1 and 11. We could then build cytometry plots displaying either counts of ND-PEI or ND-PAH per vesicle versus its size in the case of a single type of labeling (Figure 3A), or ND-PEI versus ND-PAH counts (Figure 3B) in the case of the two types of labeling. These plots are similar to the ones of image cytometry plots built from fluorescence microscopy data. The (discrete) number of fluorescent NDs of each kind is reminiscent to, but more precise than, the (continuous) luminescent intensity at a given wavelength in conventional cytometry plots. In Figure 3B the occurrence of a vesicle encompassing a given (ND-PAH, ND-PEI) count is represented by the color of the marker. Figure 3B thus gives a rapid, comprehensive and synthetic view of the data set.

In this particular proof of principle where we used two different labels (Figure 3B), several straightforward observations can be drawn. First, the pure vesicles (single type of label) are over-represented compared to mixed vesicles (labeled with two types of cationic NDs). Indeed, over the 88 investigated vesicles, 31 are filled only with PEI and 23 only with PAH. The fact that most of the internalization seems to occur with only PEI or only PAH coating is consistent with differential internalization pathways of ND-PAH and ND-PEI that we have shown in previous work¹⁷, although here the NDs are larger (150 nm instead of 50 nm). Indeed, we had observed that PAH-coated particles are mainly internalized by clathrin mediated endocytosis while PEI-coated ones are able to trigger an additional pathway, the macropinocytosis. Second, the content of mixed vesicles distributes evenly in the (number of PEI, number of PAH) space. Third, the vesicles containing a small quantity of fluorescent NDs are over-represented (about 65% with a number smaller or equal to 3 fluorescent NDs). A STEM image of a typical vesicle of this category is shown on top of Figure 3C and 3D, sparsely filled with NDs. It corresponds in this case to an endosome. Fourth, the general tendency is of course an increase of the diameter as the number of embedded NDs increases, as expected from simple steric consideration. However, the dispersion in vesicles sizes is very large for the same or similar (PEI, PAH) counts. An example of a large vesicle containing densely packed NDs is shown at the bottom of STEM images Figure 3C and 3D. This vesicle is most likely a macropinosome, considering its size, elongated form, and not well-defined delimiting membrane. Here, ultrastructure images are invaluable to identify the vesicle filling.

Recently a new fluorescence microscopy based technique was introduced to quantify the macropinocytotic index of cancer cells. It relies on labeling macropinosomes through internalization of fluorescently labeled high molecular weight dextran molecules²¹. This approach provides a better selectivity than previous fluorescence microscopy image-based techniques. Our method could be applied to the measurement of such macropinocytotic index with yet the additional advantages of combining both luminescent microscopy (with some selectivity brought by the polymer coating) and ultrastructural morphology identifications.

Let us point out that the minimal vesicle size of ≈ 300 nm that we observed is of the order of the optical diffraction limit, and can therefore be resolved by conventional fluorescence microscopy. Moreover, fluorescent NDs are known to be ideal labels for STED super-resolution microscopy²² because they can sustain the high power of the stimulated emission laser without any degradation, with a resistance even larger than the one to the electron beam of CL-STEM. Conventional or STED microscopies could be used to realize a fluorescence image-based cytometry of internalization vesicles. However, from Figure 1, Figure 2 and Figure 3 one can see that the ND labels usually do not fill the whole vesicle, so that its size and morphology cannot be extracted from NDs fluorescence in a reliable manner, while it can be inferred from a STEM scan with nanometer precision. Therefore, despite a simpler implementation of image cytometry based solely on fluorescence microscopies, such an approach does not offer a precise quantification of the vesicle size, neither of its detailed morphology including the inner composition.

Conclusion

We have demonstrated the potential of CL-STEM for combined luminescence and cell ultrastructure imaging, and have applied this technique to multicolor image cytometry of vesicles. Thanks to the diversity of emission spectra of CL-nanoprobes²³, CL-STEM should have a higher specificity than gold nanobeads of different sizes conventionally used in EM immunocytochemistry when probes are multiplexed. Though this is an advantage, the materials currently available have a few drawbacks. As in our case, a simple straightforward bicolor imaging was complicated by the presence of red emitters in the batch of green emitters. This is an issue related to purification of samples and with efforts in this direction, pure emitters are not far away. As a proof of principle application we have considered vesicular localization of two types of fluorescent nanodiamonds of with distinct CL spectral signatures after internalization. The high resolution of STEM allows acquiring images of the cellular ultrastructure both in BF and HAADF contrasts from which we can infer various information, and in particular the cross-sectional size of vesicles. By overlapping pixel-by-pixel, the STEM images with the CL emissions of internalized NDs, we could classify the vesicles depending on the ND spectral labeling. The different cationic polymer coatings (PEI or PAH) of the NDs could be used in the future in order to direct each type of ND in different vesicles. Indeed, as demonstrated in a previous study¹⁷, that NDs-PAH are found only in clathrin-related endosomes, and therefore should

label these type of endosome in CL red color. On the contrary, NDs-PEI were found in both clathrin-mediated endosomes and in macropinosomes. In order to improve the specificity of functionalized ND and direct them in macropinosomes, PEI could be replaced by dextran²¹.

More generally, using antibody-functionalized ND²⁴ combined with microinjection, it should be possible to label other intracellular organelles like mitochondria and then proceed with a detailed CL-STEM cytometry in relationship with the problem of interest (e.g. study of local temperature fluctuations measured with ND-based thermometer²⁵). Also, other types of CL nanolabels, such as II-VI luminescent semiconductor nanocrystals (quantum dots) could be used, as they also have been demonstrated to be efficient cathodoluminescent emitters¹³. Finally, with the emergence of commercial STEM-CL instruments, image acquisition and analysis automation improving the statistics, we foresee that CL-STEM novel image cytometry technique will find numerous applications in subcellular level cell biology.

References

- (1) Hell, S. W. *Angew. Chemie Int. Ed.* **2015**, *54*, 8054–8066.
- (2) Moerner, W. E. W. E. *Angew. Chemie Int. Ed.* **2015**, *54*, 8067–8093.
- (3) Betzig, E. *Angew. Chemie Int. Ed.* **2015**, *54*, 8034–8053.
- (4) Li, D.; Shao, L.; Chen, B.-C.; Zhang, X.; Zhang, M.; Moses, B.; Milkie, D. E.; Beach, J. R.; Hammer, J. A.; Pasham, M.; Kirchhausen, T.; Baird, M. A.; Davidson, M. W.; Xu, P.; Betzig, E. *Science*. **2015**, *349*, aab3500.
- (5) de Boer, P.; Hoogenboom, J. P.; Giepmans, B. N. G. *Nat. Methods* **2015**, *12*, 503–513.
- (6) Shu, X.; Lev-Ram, V.; Deerinck, T. J.; Qi, Y.; Ramko, E. B.; Davidson, M. W.; Jin, Y.; Ellisman, M. H.; Tsien, R. Y. *PLoS Biol.* **2011**, *9*, e1001041.
- (7) Cortese, K.; Diaspro, A.; Tacchetti, C. *J. Histochem. Cytochem.* **2009**, *57*, 1103–1112.
- (8) Timmermans, F. J.; Otto, C. *Rev. Sci. Instrum.* **2015**, *86*, 011501.
- (9) Liv, N.; Zonneville, a C.; Narvaez, A. C.; Efftting, A. P. J.; Voorneveld, P. W.; Lucas, M. S.; Hardwick, J. C.; Wepf, R. a; Kruit, P.; Hoogenboom, J. P. *PLoS One* **2013**, *8*, e55707.
- (10) Kociak, M.; Stéphan, O.; Gloter, A.; Zagonel, L. F.; Tizei, L. H. G.; Tencé, M.; March, K.; Blazit, J. D.; Mahfoud, Z.; Losquin, A.; Meuret, S.; Colliex, C. *Comptes Rendus Phys.* **2014**, *15*, 158–175.
- (11) Kimura, E.; Sekiguchi, T.; Oikawa, H.; Niitsuma, J.; Nakayama, Y.; Suzuki, H.; Kimura, M.; Fujii, K.; Ushiki, T. *Arch. Histol. Cytol.* **2004**, *67*, 263–270.
- (12) Niioka, H.; Furukawa, T.; Ichimiya, M.; Ashida, M.; Araki, T.; Hashimoto, M. *Appl. Phys. Express* **2011**, *4*, 112402.
- (13) Furukawa, T.; Niioka, H.; Ichimiya, M.; Nagata, T.; Ashida, M.; Araki, T.; Hashimoto, M. *Opt. Express* **2013**, *21*, 25655.
- (14) Mahfoud, Z.; Dijksman, A. T.; Javaux, C.; Bassoul, P.; Baudrion, A.-L.; Plain, J.; Dubertret, B.; Kociak, M. *J. Phys. Chem. Lett.* **2013**, *4*, 4090–4094.
- (15) Tizei, L. H. G.; Kociak, M. *Nanotechnology* **2012**, *23*, 175702.
- (16) Alhaddad, A.; Adam, M.-P.; Botsoa, J.; Dantelle, G.; Perruchas, S.; Gacoin, T.; Mansuy, C.; Lavielle, S.; Malvy, C.; Treussart, F.; Bertrand, J.-R. *Small* **2011**, *7*, 3087–3095.
- (17) Alhaddad, A.; Durieu, C.; Dantelle, G.; Le Cam, E.; Malvy, C.; Treussart, F.; Bertrand, J.-R. *PLoS One* **2012**, *7*, e52207.
- (18) Mita, Y. *Phys. Rev. B* **1996**, *53*, 11360.
- (19) Hauf, M. V.; Grotz, B.; Naydenov, B.; Dankerl, M.; Pezzagna, S.; Meijer, J.; Jelezko, F.; Wrachtrup, J.; Stutzmann, M.; Reinhard, F.; Garrido, J. A. *Phys. Rev. B* **2011**, *83*, 1–4.
- (20) Petrakova, V.; Rehor, I.; Stursa, J.; Ledvina, M.; Nesladek, M.; Cigler, P. *Nanoscale* **2015**.
- (21) Commisso, C.; Flinn, R. J.; Bar-Sagi, D. *Nat. Protoc.* **2014**, *9*, 182–192.
- (22) Arroyo-Camejo, S.; Adam, M.-P.; Besbes, M.; Hugonin, J.-P.; Jacques, V.; Greffet, J.-J.; Roch, J.-F.; Hell, S. W.; Treussart, F. *ACS Nano* **2013**, *7*, 10912–10919.
- (23) Zhang, H.; Aharonovich, I.; Glenn, D. R.; Schalek, R.; Magyar, A. P.; Lichtman, J. W.; Hu, E. L.; Walsworth, R. L. *Small* **2014**.
- (24) Chang, B.-M.; Lin, H.-H.; Su, L.-J.; Lin, W.-D.; Lin, R.-J.; Tzeng, Y.-K.; Lee, R. T.; Lee, Y. C.; Yu, A. L.; Chang, H.-C. *Adv. Funct. Mater.* **2013**, *23*, 5737–5745.
- (25) Kucsko, G.; Maurer, P. C.; Yao, N. Y.; Kubo, M.; Noh, H. J.; Lo, P. K.; Park, H.; Lukin, M. D. *Nature* **2013**, *500*, 54–58.
- (26) Su, L.-J.; Fang, C.-Y.; Chang, Y.-T.; Chen, K.-M.; Yu, Y.-C.; Hsu, J.-H.; Chang, H.-C. *Nanotechnology* **2013**, *24*, 315702.

Figures

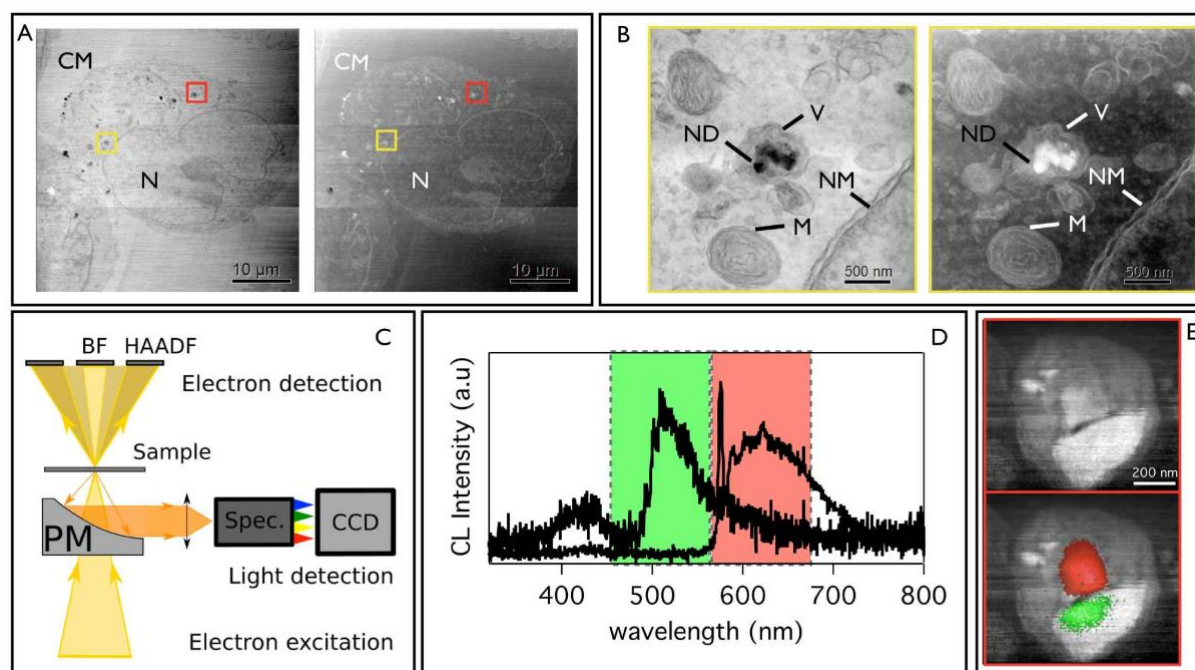


Figure 1. Correlation between ultrastructure imaging and hyperspectral imaging. (A) Left: High Angle Annular Dark Field (HAADF) and Right: Bright Field (BF) images of a whole cell (N: nucleus) with visible NDs on the cell membrane marked CM. (B) Magnified images (Left: BF, Right: HAADF) of the area framed in yellow in (A). The nanodiamond (ND) as well as ultrastructure components such as vesicles (V), mitochondria (M) and nucleus membrane (NM) are clearly distinguished in the uranyl acetate stained cell samples. (C) Schematics of the detection part of the CL-STEM hyperspectral setup. PM: parabolic mirror; Spec.: optical spectrometer; CCD: Charge Coupled Device array detector. (D) Examples of H3 (boxed in green) and NV (boxed in red) spectra, extracted from the two NDs shown in E. The NV spectrum consists in a sharp line (Zero-phonon line) followed by a convoluted series of peaks (phonon lines). (E) HAADF image, and overlapped H3 (green), NV (red) and HAADF images taken on a vesicle framed in red in (A).

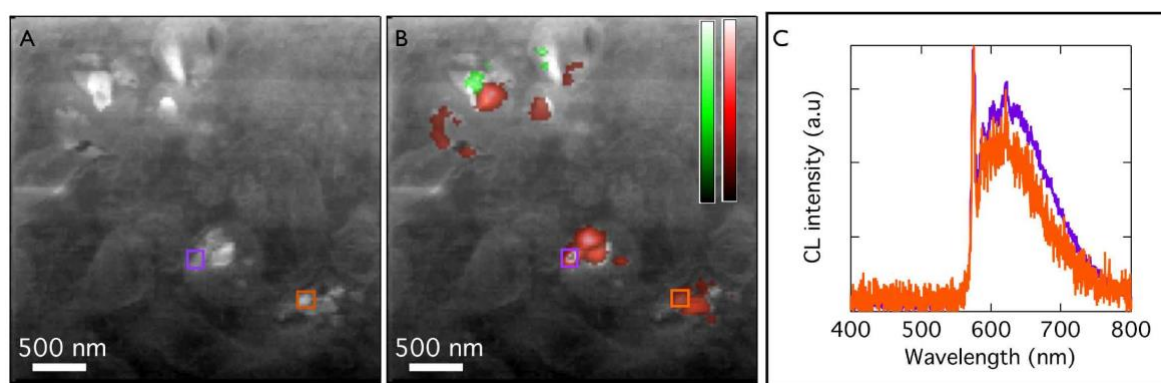


Figure 2. Disentangling NV emission as a function of coating. (A) HAADF image showing vesicles containing NDs. (B) Green and red CL emission maps extracted from a spectral image of the same area as in (A), and superimposed to HAADF image. (C) CL emission spectra of two NV-containing NDs corresponding to the violet and orange delimited areas in (A) and (B), and normalized to their ZPL maximum intensity. The phonon regions of the spectra have clearly different amplitudes, as a signature of different coatings (see text).

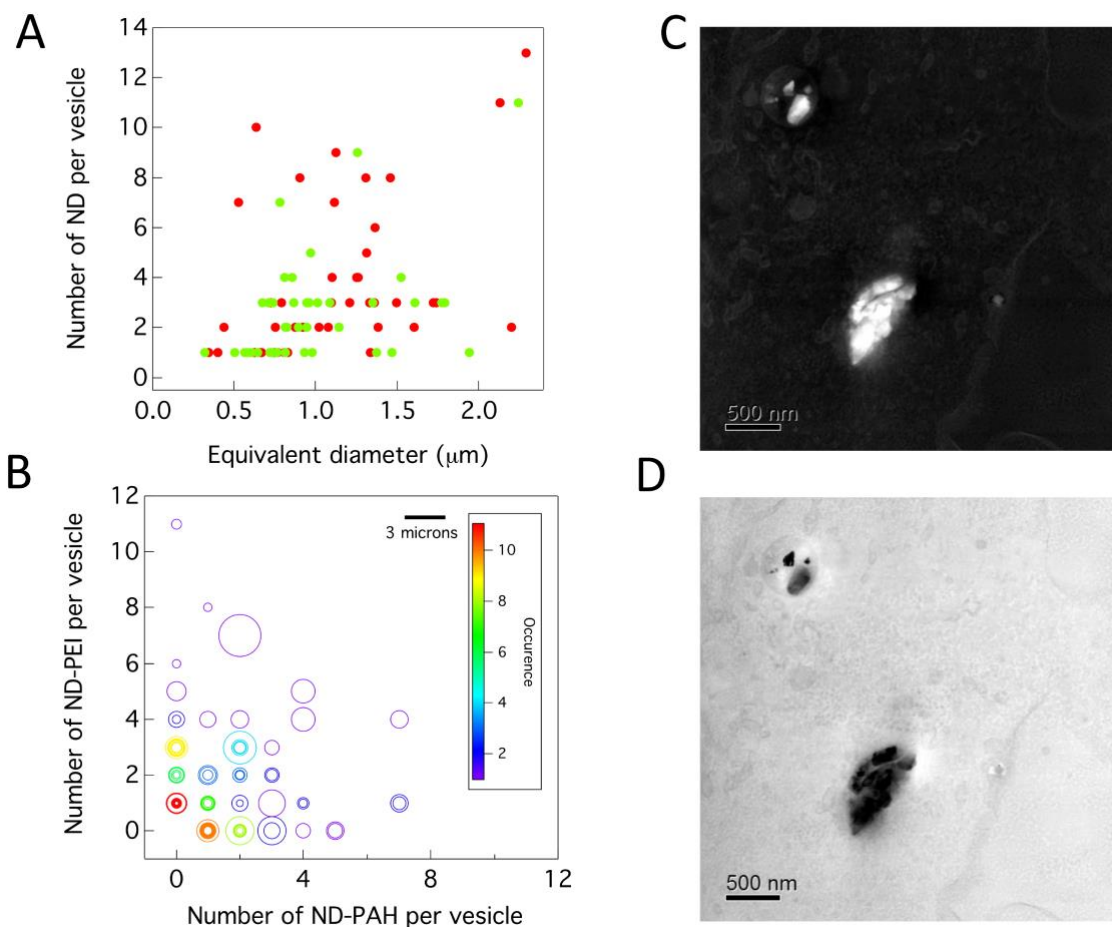


Figure 3. Cytometric plots of internalization vesicles labeled with polymer coated fluorescent NDs. (A) Number of ND per vesicle versus the vesicle size (equivalent diameter) in the case of single labeling (control sample) by either ND-PAH (red dots) or ND-PEI (green dots). (B) Double labeling by internalization of ND-PEI and ND-PAH simultaneously. Number of ND-PEI vs number of ND-PAH per individual vesicle. This plot displays also vesicles containing a single type of polymer coated ND (counts equal to 0 along the other coating axis). In the co-loaded case, we investigated 5 cells in which we detected 296 CL-emitting NDs that were distributed among 88 vesicles. The diameter of the circular markers is proportional to the vesicle size (refer to the scale bar). Different vesicles with the same number of ND-PAH and ND-PEI but different diameters appear as concentric circles. The occurrence (i.e. the number of vesicles encompassing the same number of NDs whatever its coating is) is given by the color. (C) HAADF and (D) BF STEM image showing, in the same field of view, two vesicles with different morphology and ND density: a small and round one containing a few NDs (on top), and a larger one, elongated with much more NDs inside.

Methods

Fluorescent ND preparation.

Both types of NDs were radiation-damaged with a high-energy (3 MeV) proton beam, as detailed in Su et al.²⁶. Briefly, a thin diamond film (thickness < 50 μm) was prepared by depositing ≈ 5 mg of ND powder on a silicon wafer (1x1 cm² size) and subsequently subjected to the ion irradiation at a dose of ≈ 2x10¹⁶ H⁺.cm⁻². Afterwards, the radiation-damaged NDs were annealed at 800°C for 2 h to form fluorescent NDs. To remove graphitic carbon atoms on the surface, the freshly prepared fluorescent NDs were oxidized in air at 490°C for 2 h and microwave-cleaned in concentrated H₂SO₄-HNO₃ (3:1, v/v) at 100°C for 3 h.

Cell lines.

A673 Human Ewing Sarcoma cell lines were used as the model system. These cells were cultured in DMEM with 10% FBS and 1% PS. Once the cells reached 70% confluence they were trypsinized and seeded on cover slips placed in 6 well plate. About 10⁵ cells were plated and allowed to adhere overnight. These cells were then incubated with ND-PEI and ND-PAH (100 μL each in 500 μL of medium) for 4 hours. Control cells were treated with only ND-PEI or ND-PAH for 4 hours. The co-loaded cells and the control cells were rinsed in 1X Phosphate Buffered Saline (PBS) to remove nanoparticles in excess. Cells were fixed using 2% glutaraldehyde in 0,1M cacodylate buffer, pH 7.4 for 1h at room temperature and then post-fixed for 1 hour at room temperature with 1% osmium tetroxide and 1% potassium ferrocyanide in cacodylate buffer. They were dehydrated and finally embedded in epoxy resin. The monolayer was sectioned to 200-300 nm thin section on an ultra-microtome. The sections were exposed to chloroform vapors to stretch them and reduce wrinkles. They were then loaded on carbon/collodion coated copper finder grids. For experiments of Figure 1, the whole procedure was the same except for an additional final step of Uranyl Acetate staining used to increase the image contrast.

Supporting Information

“Simultaneous cathodoluminescence and electron microscopy cytometry of cellular vesicles labeled with fluorescent nanodiamonds”

S. Nagarajan *et al.*

Contamination of Type 2 ND sample by particles containing red emitting NV centers.

In green light emitting type 2 sample we have observed the presence of red light emitting nanoparticles in addition to the green emitting ones. To determine the contamination of type 2 sample, we dispersed ND on a carbon film and imaged them by CL-STEM. Figure S1 shows that type 2 sample diamond nanocrystals displaying a CL signal contain either green (H3) or red (NV) color centers but never both in the same crystal. From the analysis of CL spectral images for 8 field of view of size 15.17 μm x 15.17 μm we inferred that 57 of type 2 ND are purely green emitters.

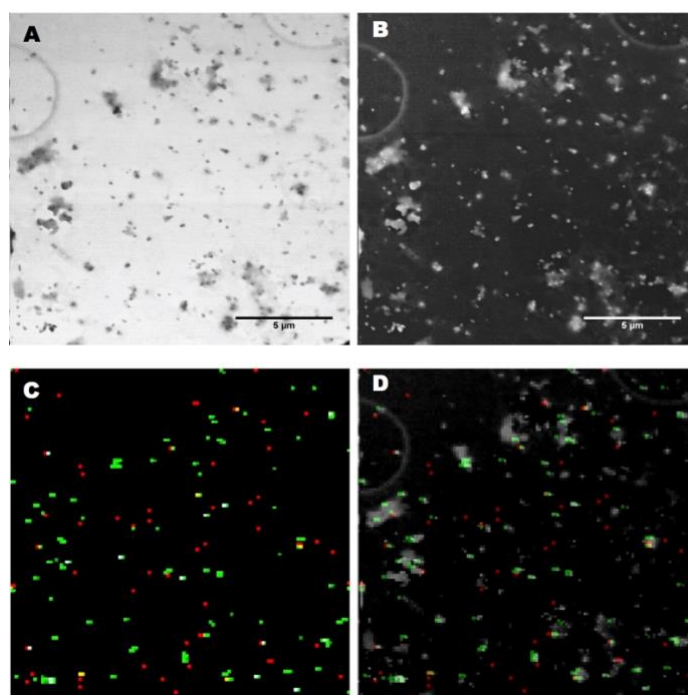


Figure S1 – Contamination of Type 2 ND sample by particles containing red emitting NV centers. (A) Low magnification bright field image of Type 2 NDs. (B), corresponding dark field image for the same region with a smaller sampling (C), corresponding CL emission. (D) Overlap of B and C demonstrating the presence of contaminating red emitters in Type 2 sample. Scale bar: 5 μm .

As stated in the main text, the Type 2 ND sample is unfortunately not spectrally pure and contains either red or green emitting nanoparticles. The red emitters are NV centers in type 1 and in type 2 NDs, and we did not observe significant CL spectrum differences in **bare** ND of both types. However, we noticed that **after cationic polymer coating**, the spectrum of embedded NV centers were modified differently, depending on the type of polymer used (Figure 2C of the main text). The phonon region is indeed significantly different in both types of NDs.

In order to distinguish between PAH-coated Type 1 NDs (which are all red emitters) and PEI-coated Type 2 red-emitting NDs, we have developed a method relying on **multivariate analysis**. Specifically, we have applied K-means analysis to the coloaded sample. This analysis has led to the discrimination of the NDs into two clusters. These clusters could be assigned to either ND-PAH or ND-PEI by comparison with the results of the same analysis done on reference samples made up of only ND-PAH or ND-PEI with *a priori* knowledge of polymer coating.

K-Means method used to identify the coating of red emitting NDs.

Principle – K-means is a clustering method that groups different data into separate clusters, based on the minimal distance between observations within a given cluster. The number of clusters is an input of the method, and thus an evaluation of the relevance of the choice of a particular number of clusters is necessary. We note that several numbers of clusters may be optimal, as sub-clustering might arise in samples. Moreover, the K-Means relying on heuristic minimizing methods, might be prone to initial condition errors, and it is therefore usually run several times with different initial conditions to avoid local minima.

In the present work, the data set is made of the CL spectra, and each cluster is centred around a centroid spectrum, from which any spectrum comprised into the given cluster is supposed to be the closest, and any spectrum comprised in any other cluster supposed to be furthest.

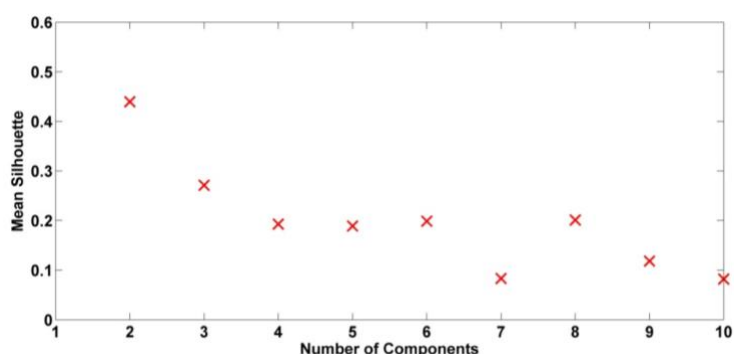


Figure S2 – Mean Silhouette for a K-Means analysis of polycation coated NDs in the coloaded samples.

Here, the criterion that is used to validate the optimal number of clusters in the sample pool is a maximal mean silhouette index¹ (Figure S2). The **silhouette index** defines how well separated the sample groups are. A high silhouette index for a given number of groups indicates that the different spectra cluster well around their centroid and are far away from the other centroids. Therefore, the optimal number of components has the maximum mean silhouette. If this optimum is reached for different number of clusters, sub-clustering is taking place. Moreover, some reports suggest a relationship between the values of the mean silhouette and the strength of the difference between samples. Values above 0.8 indicate a well defined structure, 0.5 to 0.8 presence of some structure, 0.3-0.5 weak structure and less than 0.3 might be an artefact. But these values are empirical based on observations that strongly depend on the analysed sample and cannot be used as a rule of thumb. Finally, the physical content of the output of the automatic method must be also carefully considered with respect to relevant physical parameters.

In practice, the CL spectra were analysed using the K-Means function of MATLAB statistical analysis tool box. K-Means algorithm groups the spectra in clusters for which it calculates the mean centroid spectrum representing best each cluster (see Figure S3 for an example). A minimum of 3 replicates (starting values are changed by the method in MATLAB) were run to ensure identification of a global solution by the K-means method. The number of clusters were chosen to be two, in agreement with the silhouette behaviour (Figure S2) as a function of the number of clusters, and the known physical input (i.e. the existence of two different coatings).

Applying the method of identification of the coating to blind samples – The method was first applied to cells co-incubated with ND-PAH and ND-PEI. We used K-Means to analyse CL spectra of red emitting ND only. This led to the finding of two clusters of red spectra (each presented as 2D stacks on Figure S3, left.), with their corresponding centroids represented in the centre of Figure S3. The corresponding residuals are represented on the right side, while the difference between the two centroids is shown at the bottom of Figure S3. It is clear that both centroids differ by the ratio between the phonon region and the zero-phonon line, as can be seen in Figure 2C of the main text, but here

¹ Rousseeuw, P. J. *J. Comput. Appl. Math.* **1987**, *20*, 53–65.

retrieved with limited prior information or assumption. We now need a criterion to assign a given centroid, and thus cluster to each type of coating.

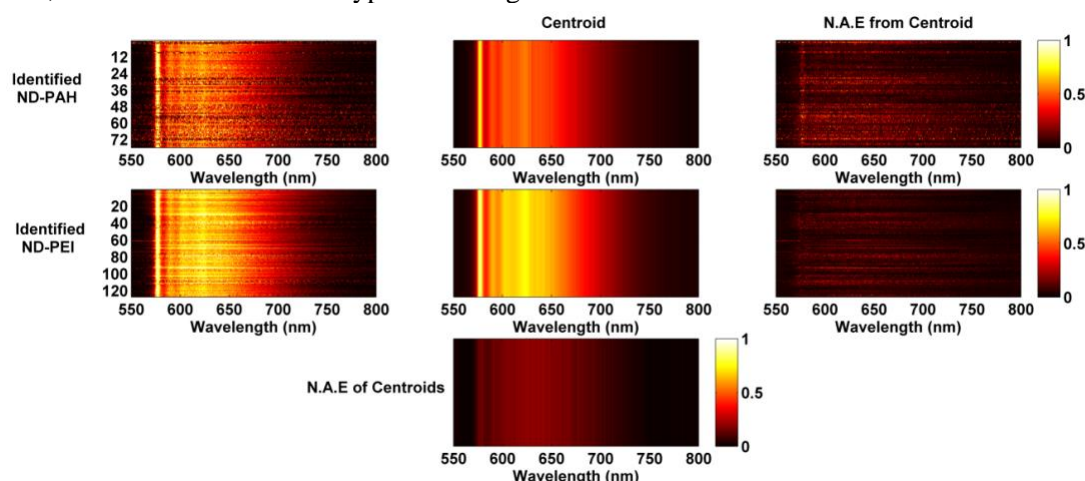


Figure S3 – K-Means analysis of CL spectra of red-emitting ND in the case of cell co-incubated with ND-PAH and ND-PEI . In this representation, each spectrum is represented as a linear image. All spectra are then stacked on each other to form a two dimensional image. This representation helps to identify differences and similarities between spectra. Top row : first cluster, further attributed to ND-PAH signature. From left to right, experimental spectra, centroid and NAE: Normalized absolute error (normalized value of the difference between experimental and centroid spectra). The centroid 2D image is the repetition of the centroid spectrum. Middle row: second cluster, further attributed to ND-PEI. Bottom: N.A.E between the two centroids .

Applying the methods of polymer coating identification to reference samples – We applied K-Means to a set of data gathering CL spectra of red emitting ND from known samples, one with only ND-PEI and the other with only ND-PAH (Figure S4). The purpose of this test was to (i) verify the accuracy of K-Means to identify clusters of each type of coated NDs and (ii) assign a typical centroid to a given coating. All the ND-PEI have been correctly assigned (100% success) while $\approx 60\%$ of the ND-PAH have been correctly assigned. Moreover, the ND-PEI centroid spectrum differs from the ND-PAH one by a larger phonon contribution. As a confirmation, we have compared the centroid spectra of red emitting ND from samples containing pure ND-PEI or pure ND-PAH, and we have observed the same differences (data not shown). Such an observation allowed us to assign each of the centroids of the co-incubated cell sample in Figure S3 to a given type of ND-coating.

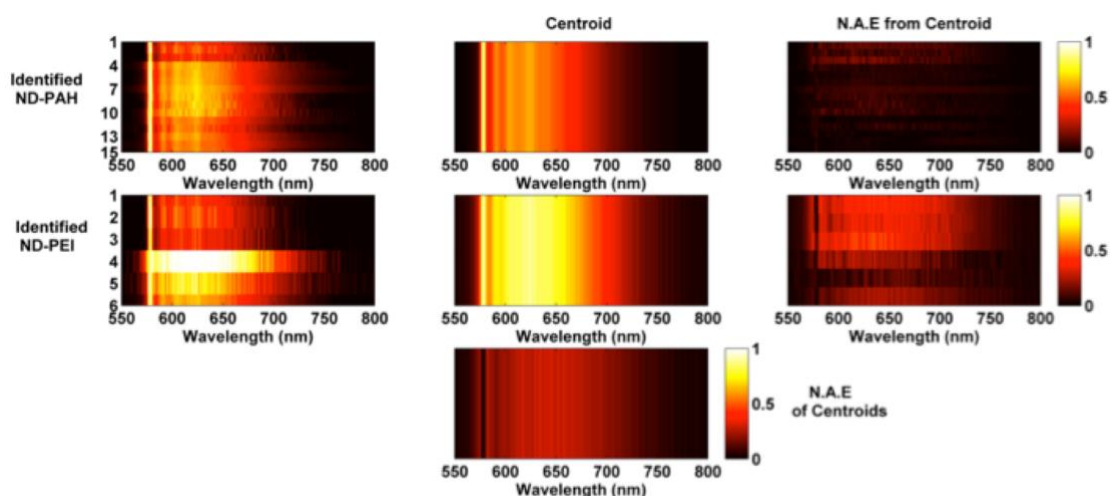


Figure S4 – K-Means analysis for the reference sample consisting of a data set made of CL spectra of nanodiamonds with known coating. K-Means is able to identify the two populations of coated nanodiamonds.

Top row : First cluster, corresponding to the ND-PAH signature. From left to right, experimental spectra, centroid and N.A.E from centroid. The centroid 2D image is the repetition of the centroid spectrum. Middle row: second cluster, corresponding to the ND-PEI signature. Bottom: N.A.E between the two centroids.
